Methods and Purposes of Aerodynamic Correlation in Formula Student

Alix Le Bastard

Division of Fluid Mechanics | Department of Energy Sciences |
Faculty of Engineering | LTH Lund University

2023

MASTER THESIS

Methods and Purposes of Aerodynamic Correlation in Formula Student

Alix Le Bastard

Methods and Purposes of Aerodynamic Correlation in Formula Student

Published by
Department of Energy Sciences
Faculty of Engineering LTH, Lund University
P.O Box 118, SE-221 00 Lund, Sweden

Supervisor, Lund University: Professor Christer Fureby
Examiner, Lund University: Professor Johan Revstedt

Abstract

Abstract:

This thesis investigates how methods of aerodynamic validation can assist a formula student team in designing their aerodynamic package. When designing their aerodynamic components, formula student team mostly rely on CFD software simulations, but there is no guarantee that the simulations depict properly the physical behaviour of the airflow around the car. For that, aerodynamic validation is a process used to compare specific CFD simulations with experiments in order to confirm the accuracy of the simulations results.

As a first step in creating validation methods for the Lund Formula Student team, a model of the LFS23 race car was designed, using a CAD software, to a scale of 1:10 that could be 3d printed as well as a S1223 airfoil shape. Experiments were conducted in a windtunnel to measured aerodynamic forces generated by the model and the airfoil at various inlet speeds or angle of attack. In parallel, CFD simulations were ran with the airfoil geometry.

The initial CFD configuration was chosen to match the one used by Lund Formula Student to design their aerodynamic package. Several parameters such as turbulence model and boundary layer meshing were tested in order to asses if the initial set of parameters was optimal for accurate results. The results of the sensitivity analysis showed that the current set of parameters used by Lund Formula Student is optimal for the CFD simulations, although new parameters could be studies, mainly for the wake refinement behind their car. Apart from the aerodynamic validation process, this thesis also aimed at showing how testing on a scaled model could prove beneficial to chose between two concept with similar performances in CFD.

Several variations of rear wing were tested in an attempt to minimise the drag generated by the car. The secondary elements of the rear wing had angles of attack ranging from 0° to -6°. After testing, it appeared that having the AoA at 0° for the secondary elements was the best configuration to minimise drag. Based on the experiment, the Lund Formula Student team trusted the results enough to run this configuration in racing conditions.

At last, an attempt of Particle Image Velocimetry experiment was made using a smoke generator and laser beams. But for various reasons, the experiment did not function. Future work could focus on designing a scaled model with spinning wheels and through the use of a custom "treadmill", the behaviour of the model would better represent racing conditions. The wake of the wheels would provide more drag, and the rolling floor beneath the car would allow for more ground effect to be generated and therefore more downforce.

Keywords: ***Aerodynamic Validation, Wind tunnel testing, CFD simulations, StarCCM+, Scaled Model, Particle Image Velocimetry***

Acknowledgements

I would like to thank Lund Formula Student and all of its members for the amazing journey the last two years. I couldn't be more proud of this experience, the hard work that everyone has put in and our amazing results achieved this year bringing back several trophies and two overall top 10 in major competitions.

I would also like to thank my supervisor Professor Christer Fureby as well as Professor Jens Klingmann for guiding me through this thesis and offering counseling and support along the way.

Thank you to Michael Johansson, Professor at the Lund University School of Aviation, for allowing me to be the first to conduct experiments in a newly arrived wind tunnel in Ljungbyhed.

Lastly, I would like to thank Lostboyslab AB for helping me 3D printing all of the parts and models I needed for my experiments. In particular, I want to thank Marcus Botha for helping me design my scaled model and teaching me a lot regarding 3D printing processes.

Table of Contents

List of Acronyms and Abbreviations

AoA Angle of Attack

BL Boundary layer

CAD Computer aided design

CFD Computational fluid dynamics

DIF Diffusor

DNS Direct numerical simulation

DRS Drag reduction system

FW Front Wing

LES Large eddy simulation

LFS Lund Formula Student

LFS23 Lund Formula Student 2023 race car

NSE Navier-Stokes equations

PDE Partial differential equation

PIV Particle Image Velocimetry

RANS Reynolds averaged Navier-Stokes

RW Rear Wing

SP Sidepods

SST Shear stress transport

Nomenclature

δ	Boundary layer thickness
μ	Viscosity
μ_t	Turbulent eddy viscosity
τ	Time spacing between laser pulses
c_d	Drag coefficient
c_l	Lift coefficient
C_p	Pressure coefficient
c_v	Molar specific heat
D	Drag
g	Gravitational constant
i	Internal energy
k	Thermal conductivity
L	Lift
l	Airfoil chord length
p	Pressure
q_∞	Dynamic pressure
R	Molar gas constant
Re	Reynolds number
S_i	Energy source term
S_{M_x}	Momentum source term
T	Temperature

u	Velocity
Φ	Dissipation function
ρ	Density

1 Introduction

1.1 Background

One of the first wind tunnel ever built was in 1901 by the Wright brothers and lead to the birth of aviation. Historically, wind tunnels and the testings conducted within them have allowed people to evaluate concepts, study fluid dynamics, measure pressure, lift or drag among other parameters.

It is only in between 1957 to 1960 that computer were first used to study fluid mechanics, namely to solve models of the Navier-Stokes equation. And this lead to the creation of CFD, Computer Fluid Dynamics, a branch now widely known with application within almost any industrial field. Of course, one of the applications, close to formula student is for Formula 1 where teams must perform an astonishing amount of simulations and minor tweaks to their concepts to extract the maximum performance.

Now that computing power have exponentially increased in the last decades, CFD simulations can take into account far more detailed models for the governing equations of fluid dynamics, run into transient modes, leading to ever more accurate results for the simulations performed.

As the simulations got more accurate with faster computing times, it has allowed engineers to test out a wider variety of concepts and run them into CFD programs to evaluate which fitted best for a given case. Compared to wind tunnel testing, where one would have to produce each design you would like to study, set-up the wind tunnel, extract the data, a longer process overall.

1.2 Lund Formula Student

Formula Student is an engineering competition. Group of students from universities across the world spend a whole year designing and manufacturing a single seater race car in order to compete during the summer during competitions.

During those competitions, each team's car will first be thoroughly investigated to verify that is rule compliant. Each team will score points based on their design process and technical choices as much as on their car performances on track.

I have involved myself in Lund Formula Student Team in Lund, Sweden, for the past two years. I spent both years working in the aerodynamic department with the objective of producing a package with the most downforce, resulting in faster lap times. I will refer to this year's car as LFS23.

Figure 1.1: LFS23 car - "Eloise"

1.3 Objectives and limits

This master thesis investigates how we can combine experiments in a wind tunnel with CFD simulations to ensure that the simulation parameters are optimal to capture the accurate physics behaviour and therefore guarantee our design will perform as expected once manufactured.

For that, the first step is to design a simplified version of our LFS23 race car, and scale it down to 10% of its initial size. The CAD design will be done on Fusion 360. Once that is done, the model will be 3d printed using Prusa iMk3 3d printers.

This model will then be used to run experiments in two different wind tunnels. The first one will allow me to measure the drag and downforce produced by the model at different inlet speeds. The second wind tunnel will be equipped with a PIV system, that will be presented later, that permits to visualise the airflow around an object in a 2D plane.

It is important mentioning that in the windtunnel, the model is attached to a planar surface, meaning that the wheels do not spin, and the floor does not move. This induces a different behaviour than in a racing context, but the physics from the experiments will be the same in the CFD simulations.

The CFD simulations will be conducted on the software StarCCM+, the main objective is to run simulations first based on our current process within Lund Formula Student and compare to wind tunnel data. The second objective with those simulations is to assess if any different CFD parameters could lead to more accurate results.

The goals of this thesis are to provide Lund Formula Student with new methods that can help them making decisions in their design period and improve their aerodynamic package performance. The first method being the correlation of CFD simulations with experimental data, to try and optimise the computing efficiency and accuracy of the simulations.

Another key goal is to showcase how a scaled model can be used to help understanding the behaviour of the car, by doing force measurements in different configurations, or using a smoke machine, once can observe the flow attachment around the surface of the model.

Lastly, I also want to prove how doing testing with the model can help choosing between different concepts of an aerodynamic component. Manufacturing a second set of sidepods in carbon fiber for our car would take weeks and resources that we cannot afford. While 3d printing a set of sidepods takes at most 6 hours, and then can be tested in a very time efficient manner. Combining 3d printing and wind tunnel experiments can be a great additional data to help choosing between concepts that would show similar performance in CFD.

2 Theoretical Framework

This section will present the needed theory to understand the experiments conducted as well as the results and the discussion. I will cover both the computational fluid dynamics processes as well as aerodynamic forces and how wind tunnel works.

A fluid can be either a liquid or a gas, it is defined as a material that continuously changes shape when subject to shear stress. Fluid dynamics is the science that predicts the motion of fluids, the applications are countless in fields such as the defense, energy, transport or motorsport industry.

In the case of the motorsport industry, engineers tackle the complex task of trying to minimise the drag of a vehicle while generating the maximum amount of downforce they can to be performant while cornering. Engineers working in the aviation field tackle the same problem, this time they try to design aircrafts that can produce the maximum amount of lift with the minimum amount of drag to reduce the fuel consumption.

The baseline to solve fluid dynamics problem has been set with the Navier-Stokes (NSE) equations in the 19th century, Claude-Louis Navier and Georges Gabriel Stokes have played a key role in developing the solving of these equations. To this day, we still use the NSE equations to describe fluid flow.

In most application cases, the flow studied is turbulent and therefore has a chaotic behaviour, this make solving the NSE equations analytically impossible. This lead to the birth of Computation Fluid Dynamics (CFD) is order to solve numerically the NSE. One could now simulate fluid flow without needing to setup rigs and perform experiments in a lab.

2.1 Governing Equations

To simulate the behaviour of a flow, a CFD software will solve the governing equations, they are describing the physics of the flow. To solve these equations, assumptions have to be made as governing equations prove to be very complex. The more assumptions are made, the quicker it will be for a CFD software to solve the equations but it also results in a lower accuracy. It is a trade-off that must always be taken into account depending on the computing power available, the time given to run CFD simulations, and the accuracy required [1].

We consider the fluid as a continuum while solving these equations, this means that its properties such as density or velocity can be described with continuous functions. That simplifies greatly the modelling of our equations. As the fluid is a continuum, it is modelled as a sum of infinitesimally small fluid particles. In our case, the scale of this fluid particles is large enough to not consider any molecular interaction. That also allows properties of the fluid such as the velocity and the pressure to be considered as averages over a large number of molecules.

The governing equations are derived from the conservation laws of physics. Namely they are the mass conservation equation, the momentum equation and the energy equation. This set of equations has more variables than equations, for that we need to one more. That complementary equation is, for a compressible flow, the equation of state.

2.1.1 Mass Conservation equation

Commonly referred as the continuity equation, the mass conservation equation states that the rate of increase in mass in a fluid element is equal to the net flow of mass across all of its faces [1].

”Nothing is lost, nothing is created” quoting Antoine Lavoisier illustrates well the mass conservation equation, for it to be fulfilled, the mass has to be conserved at all time. The equation is as follows :

$$\frac{\partial \rho}{\partial t} + \text{div}(\rho \vec{u}) = 0 \tag{2.1}$$

2.1.2 Momentum equation

The momentum equations are derived from Newton's second law stating that the rate of increase of momentum for a fluid particle is equal to the sum of all acting forces on the particle. The momentum equation for the x-direction yields [1]:

$$\frac{\partial \rho u}{\partial t} + \text{div}(\rho u \vec{u}) = -\frac{\partial p}{\partial x} + \text{div}(\mu \text{ grad } u) + S_{Mx} \tag{2.2}$$

In the equation above S_{Mx} is the momentum source term. This momentum equation for the y-direction and the z-direction are :

$$\frac{\partial \rho v}{\partial t} + \text{div}(\rho v \vec{u}) = -\frac{\partial p}{\partial y} + \text{div}(\mu \text{ grad } v) + S_{My} \tag{2.3}$$

$$\frac{\partial \rho w}{\partial t} + \text{div}(\rho w \vec{u}) = -\frac{\partial p}{\partial z} + \text{div}(\mu \text{ grad } w) + S_{Mz} \tag{2.4}$$

2.1.3 Energy equation

The energy equation states that the rate of increase of energy in a fluid particle equates the net rate of heat flowing into the particle and the net rate of work done on the particle as per the first law of thermodynamics. The energy equation is given by [1]:

$$\frac{\partial (\rho i)}{\partial t} + \text{div}(\rho i \vec{u}) = -p \text{ div}(\vec{u}) + \text{div}(k \text{ grad } T) + \Phi + S_i \tag{2.5}$$

Where k is the thermal conductivity of the fluid, Φ is the dissipation function and S is the source term.

2.1.4 Equation of state

As said before, the equation of state is needed to have as many variables as equations in our system. This equation links the density of the gas to the internal energy. Assuming an ideal gas, the equation of state is :

$$p = \rho RT, i = c_v T \tag{2.6}$$

Where R is the molar gas constant, i is the internal energy and c_v is the molar specific heat of the gas.

2.2 Turbulence

Turbulence is a flow characterised by chaotic motion of fluids through swirls and eddies of different scales. It is inherently a complex phenomena and the chaotic motion is hard to predict or resolve within numerical simulations, hence why mathematical models are used to predict its effects on flow. Within computational fluid dynamics turbulence models are commonly divided into two categories, Reynolds-averaged Navier–Stokes (RANS) and Large Eddie Simulations (LES) models.

2.2.1 RANS

All flow is governed by the partial differential equations known as the Navier-Stokes equations. By decomposing its quantities into their time-averaged and fluctuation components, the Reynolds-averaged Navier–Stokes equations can be derived. These equations govern the mean flow and serve as the basis for all RANS models and are given as [2]:

$$\frac{\partial \overline{\rho}}{\partial t} + \nabla(\overline{\rho}\widetilde{\mathbf{u}}) = 0$$

$$\frac{\partial}{\partial t}\left(\overline{\rho}\widetilde{u_i}\right) + \frac{\partial}{\partial x_j}\left[\overline{\rho}\widetilde{u_j}\widetilde{u_i} + \overline{p}\delta_{ij} - \widetilde{\tau_{ji}^{tot}}\right] = 0$$

The first equation is the (mass) continuity equation and the second equation corresponds to the conservation of momentum in three dimensional space. The Reynolds stress has here been decomposed into an anisotropic and a

isotropic part. This form of the Navier stokes equations introduces unclosed and nonlinear components, specifically in the expression for the Reynolds stress. By using Boussinesq's eddy-viscosity assumption these unclosed components are related to the mean flow of the system as [1]:

$$\widetilde{u_j}\widetilde{u_i} - \frac{2}{3}k\delta_{ij} = -\nu_T\left(\frac{\partial\widetilde{u}_i}{\partial x_j} + \frac{\partial\widetilde{u}_j}{\partial x_i}\right)$$

In other words, the Reynolds-stress now instead depends linearly on the mean velocity gradients. Here ν_T is the turbulence viscosity which requires further expressions or equations to be properly modelled. Depending on the number of additional equations used to model the turbulence viscosity, the system is usually referred to as a "number" equation model system. For example, adding one extra equation would be called a one-equation turbulence model. For this particular study the following turbulence models were used: Spalart-Allmaras, Realizable k-ε, SST k-ω, and Reynolds Stress Model. A more thorough description of these models is given below.

2.2.2 Spalart-Allmaras

Spalart-Allmaras is a one-equation model which determines the eddy turbulent viscosity based on a single viscosity-like variable, $\tilde{\nu}$, also known as the Spalart-Allmaras variable. The transport equation of this variable is given as [3]:

$$\frac{\overline{D}}{\overline{D}t}\nu_T = \frac{\partial}{\partial x_j}\left(\frac{\nu_T}{\sigma_\nu}\frac{\partial\nu_T}{\partial x_j}\right) + S_v$$

where the production term, S_v is a function of This model was originally designed specifically for aerospace applications involving wall-bounded flows. It has been shown to also give good results for situations involving boundary layers subjected to adverse pressure gradients. However, it is known to give large errors for simulations involving some free shear flows, specifically for plane and round jet flows. As an addition, it cannot properly predict the decay of homogeneous, isotropic turbulence.

2.2.3 Realizable k - ϵ

The realizable k-ε is a modified version of the standard k-ε model which is a two equation model prediction for the turbulent viscosity. The equations for the standard k-ε model are [4]:

$$\frac{\overline{D}}{\overline{D}t}k = \frac{\partial}{\partial x_j}\left(\frac{\nu_T}{\sigma_k}\frac{\partial k}{\partial x_j}\right) + P - \varepsilon$$

$$\frac{\overline{D}}{\overline{D}t}\varepsilon = \frac{\partial}{\partial x_j}\left(\frac{\nu_T}{\sigma_\varepsilon}\frac{\partial \varepsilon}{\partial x_j}\right) + C_{\varepsilon 1}\frac{\varepsilon P}{k} - C_{\varepsilon 2}\frac{\varepsilon^2}{k}$$

with

$$P = \overline{u_i^{'}u_j^{'}}\frac{\partial \overline{u_i}}{\partial x_j} \quad \nu_T = C_\mu \frac{k^2}{\varepsilon}$$

where additional constans are introduced. These constants can be obtained by solving "simple" flow systems, effectively reducing the ODEs for k and ε. They are normally given the values [4]:

$$C_\mu = 0.09, \quad C_{\varepsilon 1} = 1.44, \quad C_{\varepsilon 2} = 1.92, \quad \sigma_k = 1.0, \quad \sigma_\varepsilon = 1.3$$

The difference between the standard k-ε and the realizable k-ε is the use of a different ε equation as well as the variation of C_μ [4]:

$$\frac{\overline{D}}{\overline{D}t}\varepsilon = \frac{\partial}{\partial x_j}\left(\frac{\nu_T}{\sigma_\varepsilon}\frac{\partial \varepsilon}{\partial x_j}\right) + C_1 S\varepsilon - C_2\frac{\varepsilon^2}{k + \sqrt{\nu\varepsilon}}$$

where constants are provided as [4]:

$$C_1 = \max\left(0.43, \frac{\eta}{\eta + 5}\right), \quad \eta = \frac{Sk}{\varepsilon}, \quad S = \sqrt{S_{ij}S_{ij}}$$

This brings several improvements over the standard model, specifically for flows containing strong streamline curvature, eddies, and rotations. It is virtually superior to any standard k-ε simulation when solving for the mean flow of complex structures. The limitation is complications that arise from computing domains containing both rotation and stationary fluid zones.

2.2.4 SST k - ω

The SST k-ω turbulence model is a two-equation model for the turbulence eddy viscosity. Due to the shortcomings of the standard k-ε and k-ω models a hybrid model was created. This new SST k-ω model uses a k-ε model for free-stream flow while near-wall flow is modeled using k-ω. More specifically, k-ω is used for the inner parts of the boundary layer and is given by [5]:

$$\frac{\overline{D}}{\overline{D}t}k = \frac{\partial}{\partial x_j}\left(\frac{\nu_T}{\sigma_k}\frac{\partial k}{\partial x_j}\right) + P - \varepsilon$$

$$\frac{\overline{D}}{\overline{D}t}\omega = \frac{\partial}{\partial x_j}\left(\frac{\nu_T}{\sigma_\omega}\frac{\partial \omega}{\partial x_j}\right) + C_{\omega 1}\frac{P\omega}{k} - C_{\omega 2}\omega^2$$

where the production term, relation between ε and ωas well as turbulent eddy viscosity are given as:

$$P = \overline{u_i^{'}u_j^{'}}\frac{\partial \overline{u_i}}{\partial x_j}, \quad \varepsilon = \omega k, \quad \nu_T = C_\mu\frac{k^2}{\varepsilon} = C_\mu\frac{k}{\omega}$$

Similarly to the k-ε model certain constants are used. These are normally given as [5]:

$$C_{\omega 1} = C_{\varepsilon 1} - 1, \quad C_{\omega 2} = C_{\varepsilon 2} - 1, \quad \sigma_k = 0.5, \quad \sigma_\omega = 0.5$$

The large benefit of the SST k-ω is model that it avoids the problems of either model; k-ϵ behaving poorly at near-wall and likewise for k-ω in free-stream flow. The downside of the SST k-ω model is the over-prediction of turbulence levels in regions with large normal strains.

2.2.5 LES

Large eddy simulations (LES) are the middle ground between RANS-based models and direct numerical simulations (DNS). By using LES it is possible to resolve turbulent flows for large scale eddies. Meanwhile, the small scale effects are to be modelled. The transport equations to be resolved are [2]:

$$\frac{\partial \overline{u_i}}{\partial x_i} = 0$$

$$\frac{\overline{D}}{\overline{D}t}\overline{u_i} = \frac{\partial \overline{\tau_{ij}}}{\partial x_j} - \frac{1}{\rho}\frac{\partial \overline{p}^*}{\partial x_i} - \frac{\partial}{\partial x_j}\tau_{ij}^r$$

where the stess tensors, $\overline{\tau_{ij}}$ and τ_{ij}^r, are:

$$\overline{\tau_{ij}} = \nu \left(\frac{\partial \overline{u_i}}{\partial x_j} + \frac{\partial \overline{u_j}}{\partial x_i} \right), \quad \tau_{ij}^r = \overline{u_i u_j} - \overline{u_i u_j} - \frac{1}{3} \tau_{kk}^R \delta_{ij}$$

The overline operator here is longer the Reynolds-average but rather a filtering-spatial-and-time-average. This new average is used to determine a specific cutoff length and time scale. Eddies smaller than this length/scale are modelled. On the contrary, eddies larger than the cutoff are numerically solved through explicit calculations. The proper modelling of the small-scale eddies is important, specifically for near-wall flows, reacting flows and multiphase flows. As the cutoff length gets smaller, the LES solution become closer to the DNS solution and requires further more computational time.

2.3 Finite Volume Method

With the exception of a limited set of simplified cases, solving analytically the governing equations can not be achieved. Consequently, the governing Partial Differential Equations (PDEs) are discretized and tackled through numerical methods.

Three commonly employed techniques for solving engineering problems governed by PDEs are the finite element method, the finite difference method, and the finite volume method. In the case of Computational Fluid Dynamics problems (CFD), the finite volume method stands as the most commonly used approach. This method adopts an Eulerian frame of reference, wherein the control volume remains stationary.

The initial step involves the discretization of the fluid domain into finite control volumes known as cells, collectively forming the computational mesh. This mesh can be either structured or unstructured. Structured meshes are generally better in terms of computational efficiency and quality but are more adapted to simpler geometries.

When it comes to more complex geometries, the meshing process becomes time-consuming, leading to unnecessary refinements in intricate regions. To address these challenges, a strategy is to partition the domain into blocks, each with its structured mesh, permitting local refinement in complex areas and facilitating the capture of intricate geometries. Such meshes are referred to as multi-block structured meshes.

In contrast, the unstructured grid can be considered an extreme case of the multi-block method, where each block consists of a single mesh cell. This approach offers flexibility in dealing with complex geometries, making it a prevalent choice, as many engineering problems present complex shapes.

The flow state variables, such as velocity and pressure, are stored at the center of each cell, and the governing equations are employed to compute fluxes, including mass flow and heat flux, across cell faces. Following flux updates, new state variables are derived, and the solution's fidelity is assessed based on the compliance with the discretized equations.

The difference between the calculated and expected values, known as the residual, is computed each iteration. In a stable simulation, each iteration should yield lower residual values. Ultimately, as the residual diminishes to a sufficiently low level, the solution is deemed converged providing an iterative solution.

Finer meshes are preferred to minimize any truncation errors. However, an increase in mesh density results in a higher number of equations to be solved and a longer computing time, necessitating a delicate balance between computational cost and accuracy when selecting the mesh fidelity.

2.4 Aerodynamic Forces

When an object moves through air, an aerodynamic force is exerted upon it. These forces originates from shear stress and pressure distributions on its surface. The first is a result of viscous friction forces acting tangentially to its surface resisting movement. Secondly, the pressure distribution is a result of mass continuity and Newtons second law of motion [6]. The aerodynamic force R [N] is commonly divided into the two components of lift L and drag D, being normal respectively tangential to the velocity of the object [7].

A simplified explanation for the induced pressure distribution goes as follows: When an flow path is obstructed by an object, velocity changes to uphold mass continuity which by Bernoulli's principle, derived from Newtons second law, constitutes an opposite change in pressure (under the assumption of incompressible flow) [8].

Bernoulli's principle states that for an incompressible fluid whose density remains constant (no diffusive phenomena such as viscous forces or heat

transfer), the following quantity remains constant :

$$\frac{v^2}{2} + gz + \frac{p}{\rho} = constant \tag{2.7}$$

While encountering flow at a zero angle of attack the two aerodynamic force components are mainly composed of one source each, with lift coming mainly from the pressure distribution while the drag comes mainly from the shear stress distribution. However, when the angle in relation to incoming flow changes, the aerodynamic forces changes both in magnitude and composition. As a rule the lift is increases alongside the angle, while the drag can both increase and decrease depending on the shape. At large angles, or when the object has jagged shapes, there is a significant probability of flow separation which causes high drag and a decrease in lift due to stalling. [7].

2.5 Dimensionless coefficients

For this thesis we are working with two dimensional forces :lift L and drag D. From these forces, dimensionless coefficients are defined which are used to analyze and compare results across different scales. Both the lift coefficient c_l and drag coefficient c_d are produced by dividing their forces with the product of the dynamic pressure q_∞ of incoming flow and the reference area which itself is a product of the wing span s and chord length l. These are all defined within equation 2.8 [7].

$$c_l = \frac{L}{q_\infty l} \quad , \quad c_d = \frac{D}{q_\infty l} \tag{2.8}$$

These coefficients are utilized to characterize the performance of the airfoil or any other geometry, whose characteristics are equivalent to that of an wing with in an infinite span. In the case of an finite wing span there is effects that affect the aerodynamic force R and hence also L and D. For these, there is a separate set of coefficients denoted by large letters [7].

The pressure distribution on the surface of the airfoil can be represented by the dimensionless pressure coefficient C_p. This coefficient, defined in equation 2.9, relates the local pressure p to the dynamic q_∞ and the free stream pressure p_∞ of the incoming flow. This coefficient is commonly plotted for both surfaces along the chord within the same plot [6].

$$C_p = \frac{p - p_\infty}{q_\infty} \tag{2.9}$$

2.6 Similarity

The similarity principle a fundamental fluid mechanics concept. It is often used in experimental fluid dynamics to extrapolate or compare results obtained at one scale to another scale. This principle states that if two experimental cases are geometrically and dynamically similar, then the dimensionless numbers characterising the experiments should be equal. This allows for experiments to be conducted at a smaller scale and then extrapolate the results to predict the behaviour of a full-scale model. In order to meet the similarity criteria between two experiments, they must have the same :

1. Reynolds number $Re = \frac{\rho.u.l}{\mu}$
   It represents the ratio between inertia forces and viscous forces. This number also defines whether the flow is turbulent or laminar. If two experiments have the same Re number, they are said to be dynamically similar, and similar flow characteristics are to be expected.
2. Geometric similarity
   In order to compare an experiment with model to a full scale behaviour, the geometric shape and proportions have to be similar.
3. Other dimensionless numbers can be considered in specific cases that will not be investigated in this thesis. Namely the Froude Number (Fr), the Weber number (We) or the Strouhal number (St).

As one has to match dimensionless numbers between experiments at different scales in order to compare results, these results also have to be dimensionless. The main results that will be investigated later are the lift and drag coefficients.

2.7 Wind Tunnel

A wind tunnel is a tool that is used by aerodynamicists to study what effect the air has when moving around an object. A wind tunnel consist of an inlet section called effuser, a test section in the middle where the tested model is mounted, and then a diffuser section [9].

The air is made to move through the wind tunnel thanks to powerful fan either blowing air in or sucking air from the outlet. Wind tunnel present different categories [9], in the context of this thesis, both wind tunnel used are open return wind tunnels meaning that the air is drawn from the surroundings and rejected back into the surroundings, as opposed to a closed loop. Both of the wind tunnels are also subsonic windtunnels, and are meant to study turbulent flow.

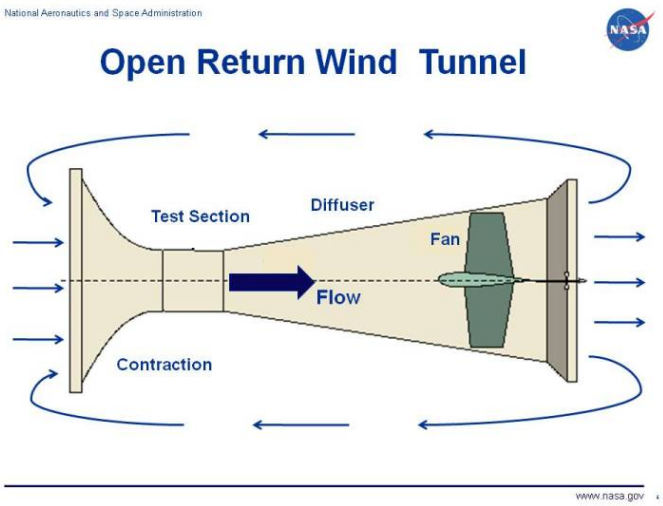

Figure 2.1: Sketch of an open return wind tunnel [10]

Various type of experiments can be conducted on models in a wind tunnel, they divide in two main categories, being either qualitative or quantitative studies. Qualitative studies mainly revolve around visualising the airflow around a test model, that can be done using smoke to observe for example is the flow remains attached to an object on all of its length. An other way is using type of paint usually called ”flow-viz” that is viscous enough to stick the model’s body while still revealing the streamlines from the air around the object.

For quantitative studies, one can use either pressure sensors with holes on the surface on an object to study the pressure distribution for example. An other type of study that can be conducted is using a force balance, using this tool one can measure the downforce (or lift) of an object as well as the drag. In the experiments presented later, I used a force balance to perform quantitative studies.

One important notion regarding windtunnel testing is the blockage ratio. It is the ratio between the frontal area of the geometry studied and the frontal area of the windtunnel's test section. Paper seem to suggest to have a blockage ratio below 16% when conducting experiments [11]. If the blockage ratio was to be higher, the interaction between the model and the walls of the test section would be significant enough to impact the aerodynamic forces generated by the model, leading to inaccuracy. In that case, corrections have to be applied to the readings to take into account the additional interactions, this will not be a problem in the experiments conducted.

2.8 Particle Image Velocimetry

The last quantitative study that I will mention in this thesis, and that I conducted, is Particle Image Velocimetry (PIV). This methods also uses a seeding generator. In this case, smoke is used as seeding particles. Instead of just observing the smoke flow, we also use lasers to track smoke particles path. It a non intrusive optical measurement method.

To perform Particle Image Velocimetry, the airflow has to be "seeded", that means that we introduce very small particles into the air. In our case the particles are produced through a smoke generator, and we assume they are small enough, meaning sufficiently low mass, so that they follow the exact same path as the air without any variation.

As mentioned earlier, this technique uses lasers. Using lenses and optical artefacts, the initial laser beam is turned into a laser plane. That laser plane has to be along the flow direction and not normal to it. It is thanks to that plane that we can visualize the seeded particles. A camera is installed in a direction normal to the laser plane to take pictures of the seeded particles at a given time.

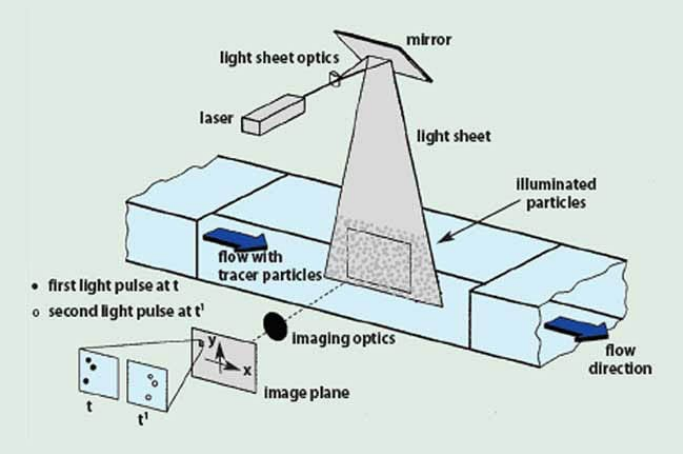

Figure 2.2: Sketch of a PIV experiment [12]

To evaluate the velocity field on that plane at a given time, there needs to be two lasers beams shot at a very short interval of time and captured by the camera. The camera is setup so that it takes a picture the moment the laser beam is shot. We then need how the particles moved between the two pictures to extrapolate a vector field for the velocity on the vector plane.

This method is called cross-correlation, the picture taken by the camera has a dimension of 1280 pixel by 1024 pixel. We now divide the ”rectangle” picture into small squares of 64x64 pixels called interrogation areas. And in each of these areas, we compare the position of the seeded particles between the two pictures. A sketch below can show how this process works.

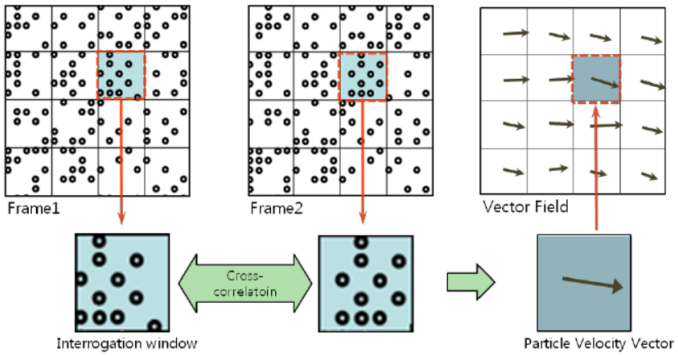

Figure 2.3: Cross-correlation sketch [13]

To estimate a velocity vector in each of the small squares, an algorithm "moves" the particles from the first picture with small d_x and d_y increments and tries to match as closely as possible the second picture taken. The process of trying all combinations of d_x and d_y is called correlation, and the algorithm looks for a peak. For each pixel square, the software can produce a map of the correlation peaks as the one below :

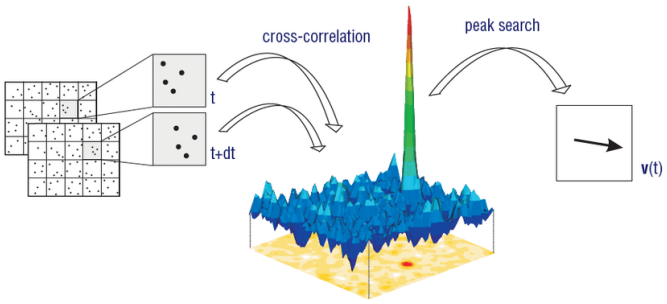

Figure 2.4: Cross-correlation peak [14]

There are seeded particles that were not in the first frame that will appear in the second frame, leading to misinterpretation from the software. To avoid that there are safety factor that can be adjusted in the software so that a vector can only be chosen if its correlation peak is significantly higher than the second highest peak.

An other common procedure to obtain better results is to chose a combination of inlet velocity and time spacing between the two lasers beams so that the average displacement of the seeded particles is less than a 1/4 of the size of the interrogation area between the two frames.

3 Experimental Method

For this master thesis I have managed to get access to two different wind tunnels, one being in Ljungbyhed and one in Lund. The objective was to run qualitative and quantitative studies to better understand the behaviour of our car as well as making sure our CFD parameters are adapted to get accurate results.

The first step to conduct those experiments was to design the model that would be tested in the wind tunnels. It had to fit in the test sections as well as having a blockage ratio of less than 5%. For these reasons I decided to design a scaled model of the 2023 Lund Formula Student car at the scale 1/10.

3.1 Scaled Model

The scaled model of our race car has been designed to resemble the model that Lund Formula Student uses to run their CFD simulations. In order to start the CFD simulations, we had to simplify the CAD of our car. For instance, we removed all fasteners, most of the suspension details while maintaining the A-arms. We also simplified the mounting of our aero components. In the picture below you can see the comparison between the 3d printed model and the CAD for the model we used to run CFD simulations :

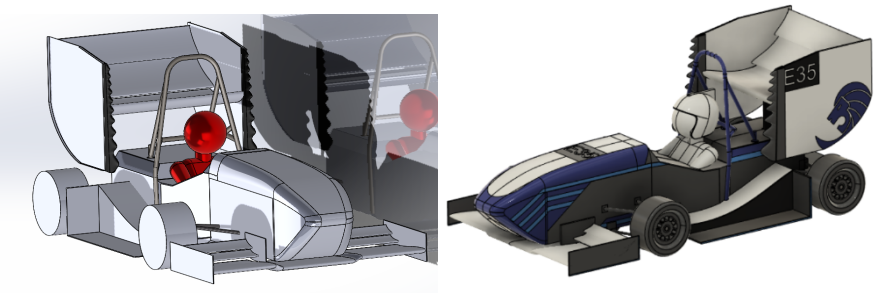

(a) CAD of the simulation model **(b) CAD of the printable model**

Figure 3.1: Comparison of both CAD models

The model has been designed so that no fastener was needed to be assembled. This means that any part can be replaced easily. There were two mains reasons behind that design feature, first if any part was to break it could easily be replaced. But the second idea I had was to later try new concept parts and study how they would perform as it would only take a few hours to print a part to study as opposed to more than 4 weeks of manufacturing for a carbon fiber part.

Also, the model has been designed so that the monocoque is the main body of the model, it is 3d printed in two halves facing upwards :

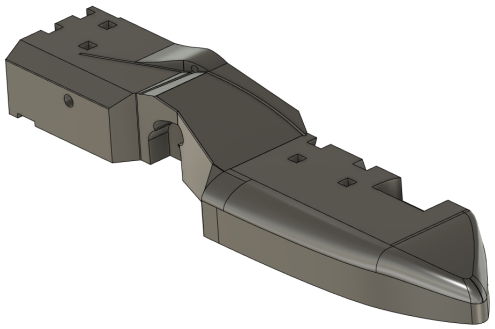

Figure 3.2: Model main body halved

One can also notice that each halve of the main body present a lot of holes, they are used to mount the rest of the parts composing the model. The spacing between the holes of the main body and the added part was chosen so that the parts fitted tightly without the need of any glue.

3.2 Ljungbyhed Wind Tunnel

The first windtunnel that I worked with is located in Ljungbyhed. The test section dimensions are 600mm*450mm*1000mm. The inlet speed could be as high as 50m/s. With the following experiments, the inlet speed did not exceed 25m/s at most as heavy vibrations started to be seen on the 3d printed components and there was a risk for their structural integrity.

Figure 3.3: Ljungbyhed wind tunnel

This wind tunnel is equipped with force transducers and an Almemo console to capture the signals emitted from the transducers. This set of equipment allows for downforce and drag to be measured.

I started my first tests by measuring aerodynamic forces on a 3d printed airfoil shape. The airfoil has the S1223 profile, with a chord length of 155mm and a width of 300mm. The mounting of the airfoil in the test chamber can be seen below :

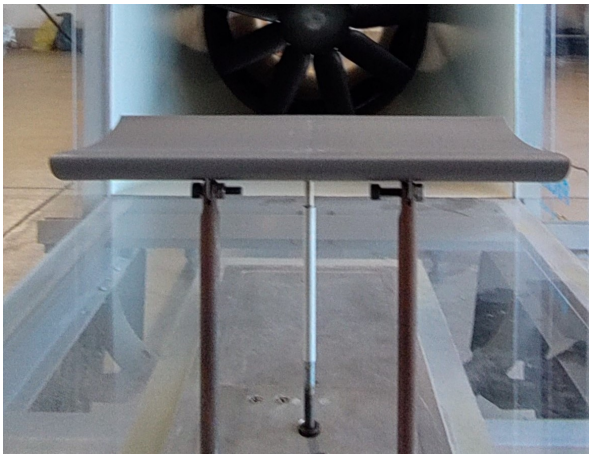

Figure 3.4: Mounting of the airfoil shape in the test chamber

The two rods that can be seen in the foreground of the picture above are connected to force transducers to measure downforce (or lift) and the third gray rod further back allow for the angle of attack of the airfoil to be changed as well as measuring the drag.

3.2.1 Measuring the AoA

When working with the airfoil shape, one of the most important parameter to measure for each experiment is the angle of attack. There was no accurate tool provided with the windtunnels. I used a CAD software to derive a relation between the height of the trailing edge and the angle of attack of the airfoil

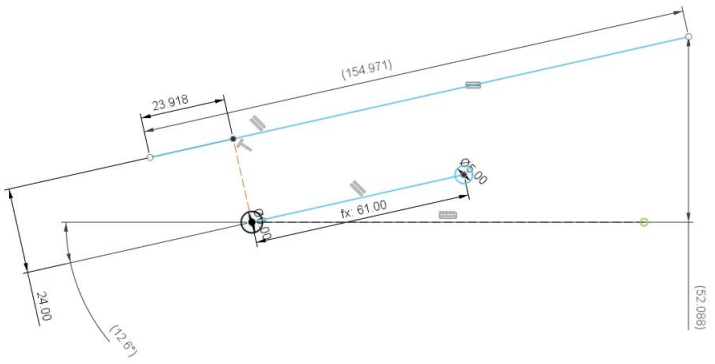

Figure 3.5: Airfoil AoA measurement setup

In the picture below, the two circles that can be seen are the mounting holes on which the airfoil is mounted. The mounting hole on the left remains static while the one to the right can move in order to change the AoA of the airfoil as presented earlier with the 3 rods. Using the CAD software, I came up with a table connecting the trailing edge height and the AoA :

Airfoil AoA	Trailing edge height (mm)
0°	207,0
2°	202,4
4°	197,8
6°	193,2

3.2.2 Sensor calibration

Apart from measuring the Angle of Attack of the airfoil, I also wanted to verify that the force sensors were calibrated. Using a delta wing mounted to the rods as a flat surface, I gradually added more weight on the wing and measured the "downforce" or weight according to the sensors.

Figure 3.6: Sensor Calibration setup

To add weight on the wing, I had access to some screws that were weighed beforehand. The screws each had a mass of 25g. I added screws to the wing by increments of 4 up to 20 screws, it provided this table :

Sensor Calibration				
Number of screws	mass (g)	Expected weight (N)	Measured weight (N)	Variation
4	100	0,98	0,98	0,0%
8	200	1,96	1,95	0,5%
12	300	2,94	2,92	0,7%
18	400	3,92	3,92	0,0%
20	500	4,90	4,90	0,0%

This small experiment proved that the downforce sensor are well calibrated, a variation of 0,7% at most is marginal. I could not repeat a similar experiment with the drag sensor as I did not know how to add a load that was in the direction of the inlet.

3.3 Lund Wind Tunnel

The second wind tunnel I had access to was located in Lund. The objective with this facility was to conduct a particle image velocimetry experiment. The setup can be seen below :

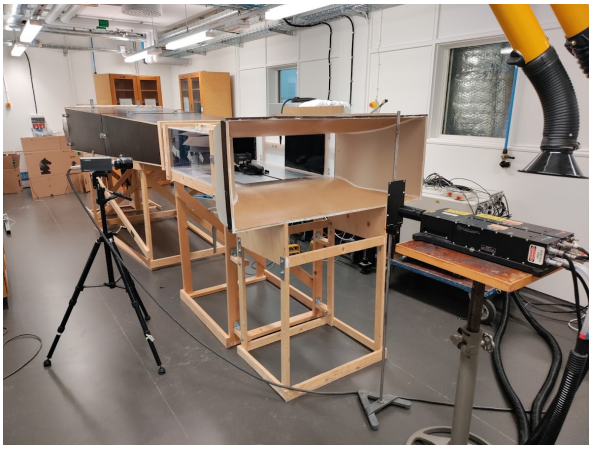

Figure 3.7: PIV experiment setup

In the picture, the wind tunnel can be seen with the model mounted in the section. The fans were positioned at the end of the diffusing section and allowed for an inlet speed of 10m/s. One can also observe the lasers on the bottom left corner of the picture, they provide short lasers beams that turn into planes through optical manipulation.

In a direction normal to the laser plane, the camera was positioned to the side of the windtunnel to capture the smoke particles moving. When conducting the experiment, the windows of the lab room were covered with cardboard to not have any outside light interfere with the lasers.

4 Simulation Setup

The objective when running the CFD simulations is to first assess whether the current simulations parameters provide results that match experimental data. In a second time, I want to change some simulations parameters, mainly regarding turbulence models and mesh generation to try and find better parameters to capture reliable results.

4.1 Simulation Domain

4.1.1 Lund Formula Student Baseline

Because of that, I chose to have the initial setup of my CFD simulations to be heavily inspired by the CFD setup ran by LFS23 to design the aerodynamic package. In the simulations ran to design the package of this year's car, the simulation domain resembles the picture below :

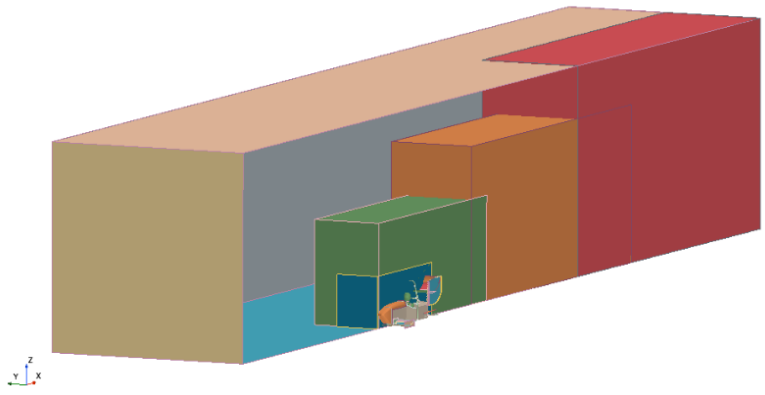

Figure 4.1: LFS Simulation Domain

The biggest "box" corresponds to the air region, half of the car can be side in the middle of the air region. There is also 4 boxes gradually bigger that are meant to perform volumetric refinement. A base size is chosen for the overall mesh and then a percentage of the base size is applied in the refinement boxes.

The boxes name are : "Car", "Near Wake", "Far Wake" and "Further Wake", the were sorted by ascending order regarding the volume and how far they are from the car. As the refinement boxes become further away from the car and wider, the percentage of the base size becomes higher, meaning that there is less refinement the furthest we are from the car. Below is the table of the percentage of base size for each refinement box :

Refinement box	Percentage of base size
Car	5%
Near Wake	25%
Far Wake	50%
Further Wake	75%

Along with these refinement boxes for the wake, we in Lund Formula Student also decided to refine the mesh around the aerodynamic components, the picture below shows the said refinement areas in pink :

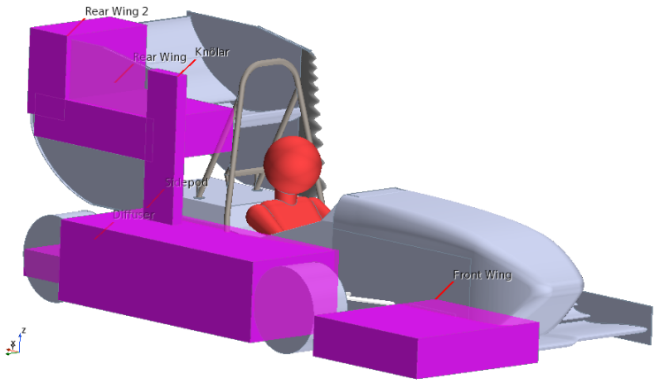

Figure 4.2: Mesh Refinement Areas

4.1.2 Current Simulation Domain

To reduce the complexity of the simulations, I decided to only have the wake refinement areas and not the ones around aerodynamic components. Instead, I chose to have a surface control applied to all of the aerodynamic components or airfoils. This was made to better mesh the boundary layer. In the initial configuration, the boundary layer is meshed with 10 prism layers. As the flow is turbulent, the thickness was chosen using the following formula [15]:

$$\delta = 0,37(\frac{l}{Re_x{}^{\frac{1}{5}}}) \tag{4.1}$$

With l being the chord length and Re they Reynolds number. In our case, the boundary layer has a thickness of $\delta = 4,7mm$ ($l = 155mm, Re = 2,6e + 05$).

The other major difference with the domain used for the LFS simulations is that they were designed to be in "free air" with symmetry conditions applied to the outside walls. While in this case, the experiments are conducted in a windtunnel with test section that has set dimensions. For that, the domain of the simulation had to be narrowed down to respect the dimensions of the test section (600mm wide and 450mm high). The domain has been chosen to be 3.5m long, this is more than 10 times the characteristic length of the tested object to ensure that the pressure of the airflow is back to the atmospheric levels by the end of the air domain. Here is a side view of the air domain as well as the airfoil positions :

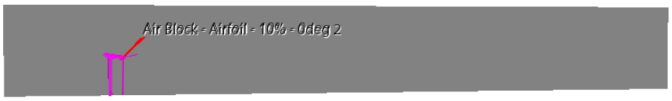

Figure 4.3: CFD Simulation Domain

Most of the simulations were ran with the airfoil geometry. I chose to do that as the simulations were less complex, meaning less computing time. But also because I ran more testing in the windtunnel with the airfoil shape and therefore felt more confident comparing the results of those experiments with CFD results to draw conclusions.

4.2 Grid generation

The mesh is generated through several operations. The first operation is a surface wrapper, using a block representing the air region, the volume occupied by the tested object (either an airfoil with the rods, or the scaled model with the delta wing) is removed from the air block.

Once this subtract operation is done, the Automated Mesh function from StarCCM+ is applied, the first step is the Surface Remesher, refining the surface produced by the CAD software and the Boolean operation that can sometimes be poor. Having done that, a polyhedral mesher is used to generate the mesh.

As mentioned in the section 4.1.1, four volumetric controls are applied to refine the wake of the tested geometry, as well as surfaces controls on any relevant component to ensure that the boundary layer is properly captured. A picture of the mesh generated can be seen below :

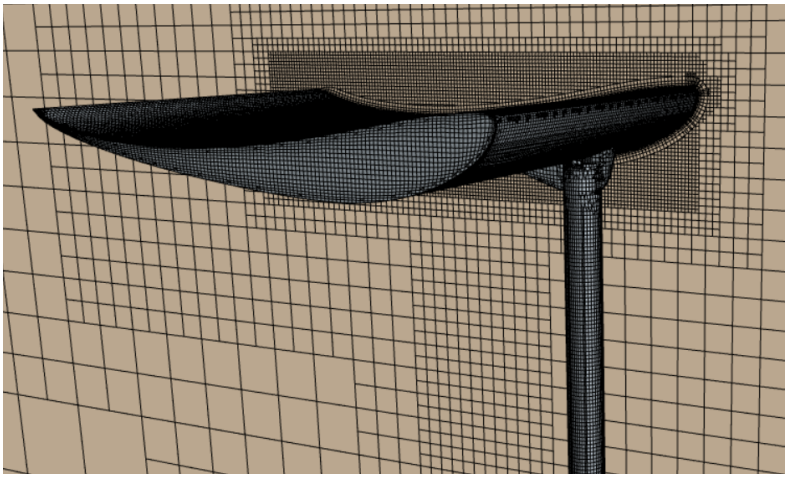

Figure 4.4: Picture of the mesh generation

The mesh generation has been designed so that the main parameter that would be changed is the base size of the cells. The refinements are made as a percentage of the base size. This allows for the generation of meshes of different sizes in an efficient manner, allowing me to conduct a mesh sensitivity analysis.

4.3 Mesh Sensitivity analysis

When running CFD simulations, the state variables of the flow are computed in the center of each cells. Once that is done, the rest of the domain is extrapolated based on the values computed in the cell centers. Running simulations with a mesh that is too coarse can lead to errors in the solution, while running simulations with a mesh that is too fine can take to much computation time to remain interesting. A balance between accuracy and computing time must be found, this is the purpose of the mesh sensitivity analysis.

For this analysis, I decided to generate 6 different meshes. As explained previously, the only parameter that will be changed between each mesh is the base size. To assess how performant each mesh is, I compare the results of the CFD simulations with experimental data obtained through windtunnel testing. Here is a table listing each base size as well as the number of cells for each mesh :

Base size (mm)	Number of cells
20	16.4 M
30	5.4 M
40	2.8 M
50	1.7 M
60	1.1 M
80	0.7 M

For each of the mesh, I chose to run 4 different cases, with different angles of attack for the airfoil (0°, 2°, 4° and 6°). For each angle of attack, the drag and downforce were measured, and then compared to the experimental data.

I then averaged the difference in aerodynamic forces between the CFD results and the experimental data. All of the simulations were ran with an inlet speed of 25m/s, the highest speed I reached during testing. Here is the table with the results :

Difference between CFD results and experimental data		
Base Size (mm)	Drag difference	Downforce difference
20	37,1 %	10,2 %
30	32,5 %	9,4 %
40	32,3 %	9,3 %
50	29,7 %	10,5 %
60	33,2 %	14,4 %
80	32,0 %	26,2 %

Following this analysis, I chose to run the following simulations with a base size of 40mm for the rest of the master thesis. As the downforce values could be trusted more, I chose for them to be the most important value to look into when choosing the most appropriate CFD parameter. One would also expect the drag difference to be reduced for each refinement of the mesh, as a finer mesh better captures the wake of the airfoil. The wake is responsible for most of the drag generated by the airfoil as well. I did not find an explanation the the increase of drag difference for the 20 mm base size compared to the rest.

The base size of 40mm proved to be the best balance between the accuracy of the results, and the computing time. It can already be mentioned that the difference is drag is very high between CFD and experimental data, but that will discussed in the Results section.

4.4 Physics setup

Once the sensitivity analysis was conducted and the simulation setup chosen, I can now explain how the physics is described for the model. The air in the region is assumed to be an ideal gas, the equation of state is :

$$P = \rho RT \tag{4.2}$$

The initial turbulence model used is the SST k-omega model. A turbulence model sensitivity analysis will be carried out later in the thesis as well. The

initial velocity of the continuum is 25m/s towards the outlet.

For the boundary surfaces of the region, all surfaces from the tested model are considered as walls with a non-slip conditions. All of the side walls, as well as the "floor" and the "roof" of the test section are considered as walls with a non-slip condition and no symmetry.

The velocity inlet is set to 25m/s once the simulation starts, and the pressure outlet is set to be the atmospheric pressure. To solve the flow and energy equations, a segregated approach was used. The SIMPLE algorithm was used to couple the velocity field and the pressure field. All of the simulations were ran in a steady state.

5 Results

5.1 Airfoil Force Measurements

The first experiment I conducted for this master thesis was using the 3d printed airfoil shape I presented earlier in the section 3. As a reminder, the airfoil has the profile of a S1223 wing element, it has a chord length of 155mm and is 300mm wide. It was designed to be mounted directly to the rods connected to the force transducers to measure the drag and downforce generated.

Figure 5.1: Airfoil experiment mounting

I decided to conduct the force measurements at 5 different inlet speeds ranging from 5m/s to 25m/s with an increment of 5m/s between each. In order to rely on the results, the sensor calibration was performed beforehand as presented in the section 3. Thanks to a feature in the Almemo console, the measurements were averaged over a period of more than 30 seconds, until

the measurements settled around a set value, to once more ensure reliable results.

This process was carried for four different angles of attack ranging from 0° to -6°. I wanted initially to have a wider range of AoA, with a higher increment but I was limited by the installation. It could have proven more interesting to capture higher AoA where the airflow starts to detach from the airfoil, and see if the results from CFD simulations could match windtunnel data.

I have gathered all of the measurements in the two tables below, one presents all of the downforce measurements, and the other one for the drag measurements. As the windtunnel was initially designed to study aircrafts, the force balance did not provide the downforce value but the lift. The only difference being its sign, I just had to inverse the values read on the console to obtain the following table :

Airfoil downforce measurement (N)				
Inlet Speed	0° AoA	2° AoA	4° AoA	6° AoA
5 m/s	0,36	0,50	0,07	1,25
10 m/s	0,65	1,02	0,16	1,40
15 m/s	1,67	1,67	1,11	2,05
20 m/s	2,94	2,68	2,76	2,74
25 m/s	4,50	4,20	4,43	3,75

Airfoil drag measurement (N)				
Inlet Speed	0° AoA	2° AoA	4° AoA	6° AoA
5 m/s	0,27	0,27	0,22	0,22
10 m/s	0,73	0,64	0,56	0,58
15 m/s	1,28	1,11	1,05	1,03
20 m/s	1,91	1,74	1,62	1,59
25 m/s	2,69	2,44	2,24	2,20

These experiments were mainly conducted to provide a reliable dataset that could then be used to compare the performance of different turbulence model or meshing parameters in the CFD. I chose to run those experiments with an airfoil shape as it was easier to print, and it will also be easier to mesh the shape in StarCCM+.

5.2 Turbulence Model CFD

Following this first experiment in the windtunnel, I started my first CFD simulations. At first I conducted the mesh sensitivity analysis that was presented in the section 4. As a reminder, I chose to run a mesh that had a base size of 40mm, meaning that the number of cells was 2,8M. The choice of that specific base size was made by comparing the CFD results to the data presented above at 25m/s, averaged for all 4 AoA tested.

This mesh with a 40mm base size will now be referred as the standard case in the tables presented in this section and the following. This standard case was ran with the SST k-omega for the turbulence model. The first comparison that I wanted to conduct was to see how other turbulence model would perform compared to the standard case.

As a reminder, the SST k-omega was the starting point for the turbulence model because it is the one that is currently used when we run simulations to design the Lund Formula Student aerodynamic package. I decided to conduct simulations with two other turbulence models that were presented earlier in the section 2 : the realisable k-epsilon model and the Spalart-Almaras model.

In the same spirit as for the mesh sensitivity analysis, I ran 4 simulations for each turbulence models. The inlet speed of all 4 simulations is 25m/s, the difference between each is the AoA of the airfoil, ranging from 0° to 6° to compare with the measurements presented earlier. I then compare the results from the CFD to the windtunnel data, and the table below presents the averaged difference each set of 4 simulations :

Downforce Measurement (N)		
Turbulence model	Mesh Size (Cell count)	Difference Windtunnel/CFD
SST k-omega	2,8 M	9,35%
Realisable k-epsilon	2,8 M	11,85%
Spalart-Almaras	2,8 M	12,85%

Drag Measurement (N)		
Turbulence model	Mesh Size (Cell count)	Difference Windtunnel/CFD
SST k-omega	2,8 M	32,34%
Realisable k-epsilon	2,8 M	21,98%
Spalart-Almaras	2,8 M	40,35%

5.3 Fine Tuning Mesh CFD

Trying different turbulence models was my first attempt to see how a difference in CFD parameters could potentially provide a better accuracy in the CFD results. I also wanted to evaluate how different meshing parameters could perform and I chose to focus specifically on the meshing of the boundary layer around the airfoil.

In the standard case, the boundary layer has a thickness of 4,6mm and is meshed with 10 prism layers. To change that meshing, I chose to first run simulations with a boundary layer half as thick and twice as thick, while keeping the same amount of prism layers. This provided the following tables :

Drag Measurement (N)		
Parameter changed	Cell count	Difference Windtunnel/CFD
Standard case	2,8 M	32,34%
Half Thickness BL	2,8 M	28,16%
Twice thickness BL	2,8 M	31,64%

Downforce Measurement (N)		
Parameter changed	Cell count	Difference Windtunnel/CFD
Standard case	2,8 M	9,35%
Half Thickness BL	2,8 M	16,90%
Twice thickness BL	2,8 M	11,19%

Having done this first set of simulations, I then chose to keep the same boundary layer thickness as it was initially but now change the number of prism layers used to mesh it. Changing that parameter will change the mesh size more significantly than the BL thickness alone, that is reflected in the number of cells in the mesh but can also clearly be seen visually when comparing all 3 meshes.

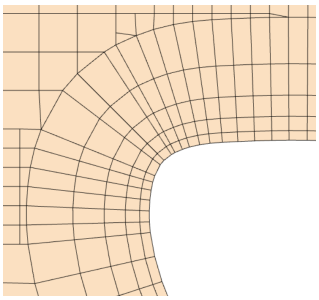

Figure 5.2: BL mesh - 5 prism layers

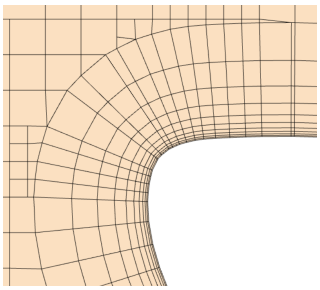

Figure 5.3: BL mesh - 10 prism layers

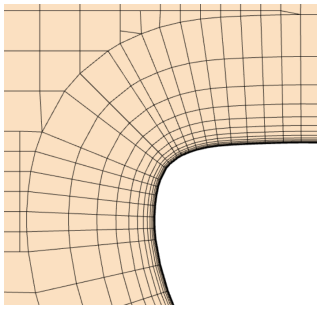

Figure 5.4: BL mesh - 15 prism layers

The result from the simulations with a varying number of prism layers can be found here:

Drag Measurement (N)		
Parameter changed	Cell count	Difference Windtunnel/CFD
Standard case	2,8 M	32,34%
5 prism layers BL	2,4 M	1,93%
15 prism layers BL	3,2 M	32,92%

Downforce Measurement (N)		
Parameter changed	Cell count	Difference Windtunnel/CFD
Standard case	2,8 M	9,35%
5 prism layers BL	2,4 M	17,91%
15 prism layers BL	3,2 M	8,92%

5.4 Scaled Model Experiments

5.4.1 Model Force Measurements

Apart from the experiments in the windtunnel with the airfoil shape and the CFD simulations that were run to try and improve their accuracy, I also spent some time doing experiments with the 3d printed scaled model of our LFS23 car. As a reminder, the model is printed at the scale 1:10.

I was advised not to change the mounting of the rods that were connected to the force transducers, as presented in the section 3, I had to mount the model to a delta wing that served as a support and a flat surface to stick the small car on. To prevent the model from flying into the fan blades, I had to use double sided tape below each wheels of the model. This will affect slightly the ride height of the model (understand the distance between the delta wing "floor" and the bottom of the model's monocoque), but I wanted to make sure the model could not detach itself from the surface at higher inlet speeds. This was how the model was fastened :

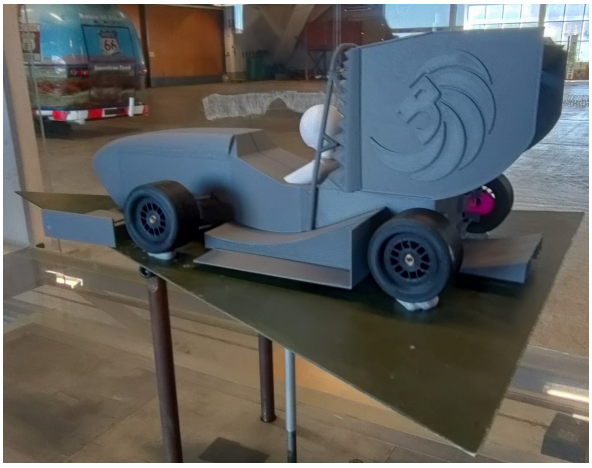

Figure 5.5: Scaled Model Fastening

Having the model taped to the delta wing support, my objective is to measure the downforce and the drag generated by the model alone in different configurations. For each measurement, I made sure that the angle of the delta wing compared to the bottom of the test section was 0°. In order to only measure the force generated by the model, I first had to measure the forces generated by the delta wing at an AoA of 0° for the 3 inlet speeds I could run with which were 5m/s, 10m/s and 15m/s.

From these values, I now had to measure the forces generated by the model and the delta wing and remove the values from the table below to only extract the aerodynamic forces produced by the model. As I presented earlier in the section 3, the scaled model has been designed to easily change or remove any component, for that reason I decided to compare how the model behaved with the whole aerodynamic package printed, and then gradually removing components.

The first component I removed was the diffusor, then the sidepods and then both the front wing and the rear wing so that no aerodynamic components were on the car. The two tables below compile the aerodynamic forces forces generated by the model at 15m/s in all of the configurations listed previously.

Drag Measurement - 15 m/s inlet speed - Scaled Model		
Model Setup	Drag measured	Cd value
No Aero	0,35 N	0,309
FW + RW	1,13 N	0,727
FW + RW + SP	1,23 N	0,750
FW + RW + SP + DIF	1,34 N	0,816

Downforce Measurement - 15 m/s inlet speed - Scaled Model		
Model Setup	Downforce measured	Cl value
No Aero	0,66 N	0,574
FW + RW	3,49 N	2,233
FW + RW + SP	4,12 N	2,506
FW + RW + SP + DIF	4,60 N	2,798

Along with the forces measured, I included the values of the aerodynamic coefficients. In motorsport, especially in formula one, one of the key target is to maximise the downforce generation while minimising drag. This means that the higher the Cl/Cd value is, the better the car performs. I compiled the Cl/Cd values of each model configuration in this table :

Aerodynamic Forces Coefficient - 15 m/s inlet speed - Scaled Model			
Model Setup	Cd Value	Cl value	Cl/Cd
No Aero	0,309	0,574	1,859
FW + RW	0,727	2,233	3,072
FW + RW + SP	0,750	2,506	3,338
FW + RW + SP + DIF	0,816	2,798	3,427

5.4.2 Drag Reduction System

Measuring the aerodynamic forces of the scaled model in different configurations was my ambition from the start. Having an estimation of how the car performs was the first step, but I also wanted to prove that with this tool, our Formula Student Team could quickly test some design idea's performance.

While running CFD simulations proves to be very time efficient to try a wide variety of designs and then optimise a certain concept, there are some times where it is hard to decide between two design options. With the budget that a team like ours has, it would prove impossible to manufacture two rear wings for example, or two different sets of sidepods and test on track to see which is best. One should also take into account that manufacturing carbon fiber components is a long and tedious task that can require up to several weeks.

The advantage of using a scaled model is that 3d printing a new rear wing or sidepods at a scale of 1:10 is a matter of a few hours at most. As differences between CFD simulations and wind tunnel data have been observed before, I am convinced backing some CAD designs with some experimental data would give us more confidence in choosing a specific aerodynamic concept.

To prove my point, I chose to design and 3d prints 4 new rear wings. Inspired by the Drag Reduction System that exists in Formula 1 for the last 12 years, I chose to change the Angle of attack of the second and third wing elements of our rear wing. The AoA of the secondary elements are ranging from 0° to -6° with an increment of 2° between each.

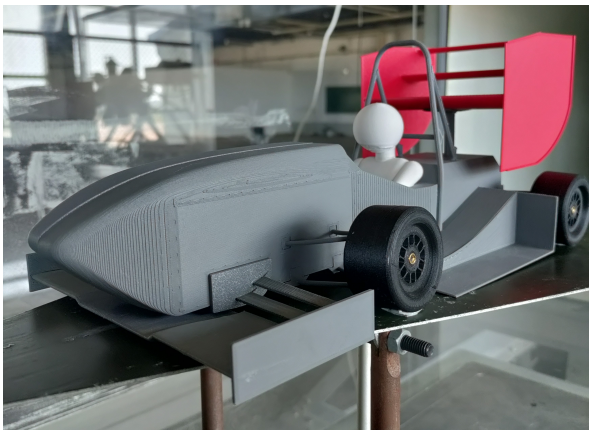

Figure 5.6: Drag Reduction Rear Wing

The objective when having the secondary wing elements flat is to minimise the drag, not only does it allow for a better straight line speed, but it can also help reducing the energy consumption of our car, which can prove needed in certain contexts that will be presented later.

Drag Measurement - 15 m/s inlet speed - DRS Rear wing		
Secondary element AoA	Drag (N)	Cd
0°	0,483	0,320
2°	0,564	0,374
4°	0,6	0,398
6°	0,485	0,322

5.5 Particle Image Velocimetry

My last objective with this master thesis was to try a Particle Image Velocimetry experiment at least once. This process is quite advanced and requires a lot of preparation, as the explanations in the section 2 can testify. After assembling the windtunnel in Lund and preparing all of the components, the scaled model was fastened to the floor of the test section in a similar manner as the previous experiments, using a double sided tape.

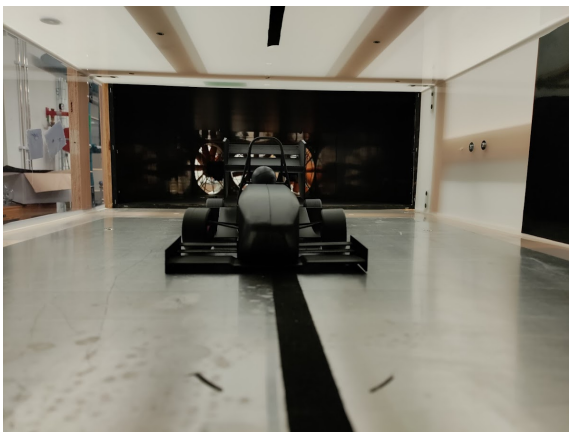

Figure 5.7: Fastening of the scaled model - Lund windtunnel

One can notice that the model has a different color than before. I had to spray paint the model using a black paint, the reason being that when doing PIV experiments, we want to setup the camera optics settings so that only the smoke particles hit by the laser can be seen in the pictures.

Adjusting the contrast of the camera settings as well as controlling how much light gets into the camera helps to have a better image quality but having the whole model black contributes more to contrast and only observe smoke particles.

The setup of the experiment was presented earlier in the section 3, an incident laser plane is generated in front of the car, and the camera is placed on the side so that the laser plane is orthogonal to the camera direction. The laser plane has to be along the flow direction, otherwise it would not be possible to observe the particle's path. For this experiment, I chose to have the laser plane going through the middle plane of the car as such :

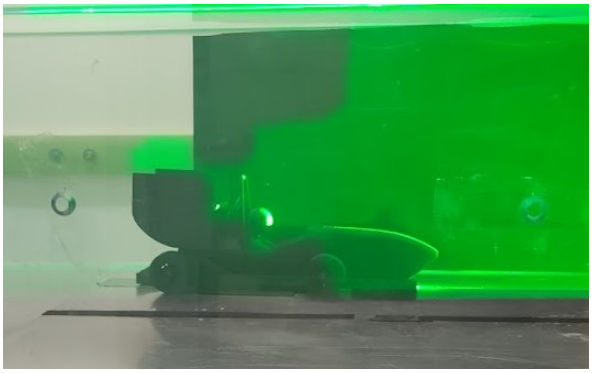

Figure 5.8: Laser plane - Scaled model

The camera has a resolution of 1280x1024 pixels. The camera and the model were positioned respectively so that the picture corresponded to a rectangle of 212mm by 163mm on the scaled model symmetry plane. This meant that each pixel corresponded to a square with a side length of 0,16mm in the symmetry plane.

Once the fans are turned on and the air starts flowing, the inlet speed is $v_{in} = 10m/s$. As a reminder from the section 2.9, the short time spacing between the two lasers pulses had to be chosen so that the particles do not move more than a 1/4 of an interrogation area between the two pulses.

For my experiment, I chose to have the interrogation area be 64x64 pixels, meaning 10,24mm x 10,24mm on the middle plane of the model. Let's name τ the time spacing between the pulses and $l = 10,24mm$ the length of the interrogation area, then we need to have :

$$\tau = \frac{l}{4}\frac{1}{v_{in}} \tag{5.1}$$

This gave a time spacing between lasers pulses of :

$$\tau = 256\mu s \tag{5.2}$$

I initially wanted to have a camera positioned so that the picture would include the whole car but that was not possible given the lab room configuration. Instead, the pictures taken captured the airflow from the front of the car until the main hoop.

With every element calibrated, I started my PIV experiment by turning on the fans and the lasers. Then a smoke machine started to blow and smoke went through the inlet. The camera took 4 sets of pictures per second, and I let it run for 5 minutes. I had to stop the smoke machine after two minutes because the room completely filled with smoke. A picture of the lab after the first few minutes can show how foggy the lab room got :

Figure 5.9: Lab room filled with smoke

Because of how much smoke was in the room, I had to stop my experiments as I feared I would trigger fire alarms. Unfortunately, the pictures taken by the camera did not reveal much and the results were not exploitable. I still decided to run the cross-correlation process on the sets of pictures taken, and the average the velocity vectors that the software estimated. This result is wrong, but proves that an attempt was made.

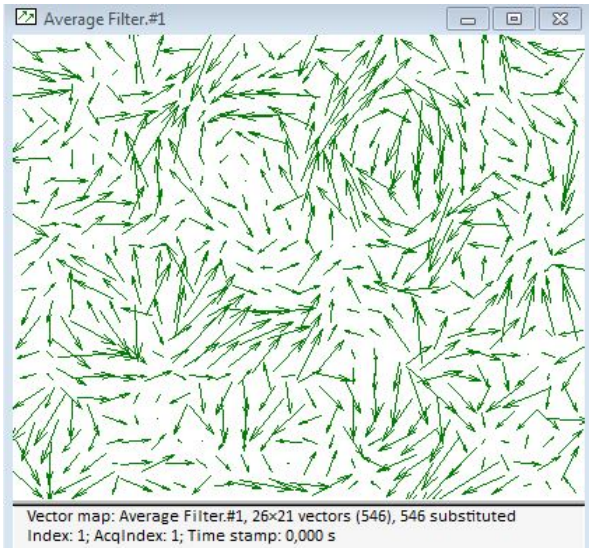

Figure 5.10: Average velocity vector map

This picture represent the averaged velocity vector in each interrogation cells of 64x64 pixels over 5 minutes. If the experiment worked, the bottom left part of the picture should not have any velocity vector as it is where the scaled model was located. I did not have more time to try and better this experiment although I think it is possible, I will discuss more on what could be improved in the next section.

6 Discussion

6.1 S1223 force measurements

For a 3d printed S1223 airfoil with a chord length of 155mm, and an inlet speed of 25m/s, the Reynolds number is Re = 2,6e+05. I have found a paper that worked on the specific S1223 airfoil shape and plotted the lift characteristics for a Reynolds number Re = 2e+05. Although I have some level of confidence in my experimental data, being able to compare my results with a published paper [16] provides an additional level of trust towards my results granted they are matching. I have made a table that contains the lift characteristics of the S1223 wing element based of the paper :

S1223 Lift characteristics - Re=2e+05	
Angle of Attack	Cl
0°	1,15
-2°	0,85
-4°	0,35
-6°	0,08

Using my own data provided in the section 5.1, I came up with this table :

Experimental S1223 Lift characteristics - Re=2,6e+05			
Angle of Attack	Downforce (N)	Frontal Area (m^2)	Cl
0°	4,50	7,04e-03	1,58
2°	4,20	7,52e-03	1,38
4°	4,43	8,07e-03	1,36
6°	3,75	8,71e-03	1,07

In fluid dynamics, the similarity principle (section 2.5), states that if the Reynolds number and the geometry of 2 separate experiments are the same, then the results can be compared. The results that can be compared can only be dimensionless coefficients, in this case the lift coefficient. While the Reynolds number are not exactly the same, they are sufficiently close to compare results.

The initial Cl value at 0° is significantly higher than the one found in the literature, and the steady decline in Cl value with the increase of the AoA is not occurring in my experiments. That could be explained by the setup of the experiment.

In my experiment the airfoil was mounted to generate downforce, while in the paper, it was placed in the opposite configuration, to generate lift. If one looks closely into the mounting of the airfoil in my case, the mounting points were positioned in the low pressure region of the airfoil. Disturbing the airflow in that very sensitive area impacted the generation of downforce and therefore the quality of the results.

One should also consider that these airfoils are meant to be more performant as the Reynolds number increases (Re=2e+05 being a relatively low value), it is then not surprising either that my Cl values are higher than the one published in the paper.

Having been able to compare some of my experimental data to a published paper gave me sufficient confidence in my downforce readings. I have not found any relevant data regarding the drag coefficient of the airfoil, and the readings are in my opinion a bit high.

I suffered a calibration reset of the drag sensor during one of my experiments and I have not found a way to make sure it was properly calibrated afterwards. Therefore when comparing CFD results with experimental data later, I mostly was interesting in the Downforce results to chose one CFD parameter variation over an other.

6.2 Turbulence Model Sensitivity Analysis

The turbulence model sensitivity analysis was the first comparison between CFD results and experimental data from the windtunnel. As specified in the last section, when comparing the CFD results to the data I measured, I mostly focus on the downforce readings as I have a lot more trust in these results.

The initial simulation case used the SST k-omega model and I tried two different turbulence model : the realisable k-epsilon as well as the Spalart Almaras. Based on the results provided in the section, it seems that the SST k-omega provided the closest results compared to experimental data.

As a reminder, the simulations were ran for all 4 AoA tested and then averaged, because of that I chose to keep the SST k-omega model for the turbulence model and I believe it is the turbulence model that should be kept for the Lund Formula Student simulations as well.

I chose not to include scalar scenes where the pressure distribution or the velocity magnitude field would be plotted because in my master thesis work, I really wanted to emphasise on how the experimental data can help chose the best CFD parameters in order to reach the highest order of accuracy in our results.

I did not have any relevant data to use to compare how the turbulence models predicted the airflow behaviour given that the PIV experiment was not successful. Hence why I chose to focus only on the data I had as a baseline for the comparisons.

6.3 Boundary Layer Mesh Sensitivity Analysis

For this thesis, I did not want the turbulence model to be the only parameter that would be changed and tested to try and optimise the CFD results. For that reason, I chose to also focus on the boundary layer meshing in particular. The initial boundary layer thickness was calculated according to the airfoil dimensions and the inlet speed.

When reducing by half or doubling the thickness of the boundary layer, the difference between the CFD results and the experimental data increased. When reducing by half the thickness of the boundary layer refinement in the mesh, the outer half of the boundary layer is meshed more coarsely, leading to more inaccuracy. While if the boundary layer thickness is doubled, there is less refinement where the boundary layer really is and a portion of the free stream is refined for no reason, leading again to a greater inaccuracy.

Thanks to these observations and results, I can confirm that our meshing of the boundary layer is correct regarding the thickness. For the same thickness, I also decided to change how many prism layers were used (meaning how many cells). When diminishing the number of prism layer the results were drastically lower but with 15 prism layer instead of 10, the results were better than the initial case.

The CFD engineers at Lund Formula Student could look into applying that parameter change in the simulation setup in order to have closer result. One thing to bear in mind is that increasing the number of prism layers result in an increase of the cell count. In my case the mesh does not contain so many cells but when meshing a whole race car accurately, the mesh has more than 100M cells.

Having a finer boundary layer meshing could provide better results, but also a few more millions of cells in the mesh and a longer computing time. This is the dilemma of any CFD problem about finding the right balance between meshing refinement and computing time, I will leave the solving of that problem to the LFS24 aerodynamic subteam.

6.4 Scaled Model Experiments

6.4.1 Model Force Measurements

The main comment that can be done regarding the scaled model experiments is that they do not reflect the actual behaviour of the car. In order for the car to remain stable, the wheels had to be taped to the delta wing surface. This meant that the wheels were not spinning while when a race car drives, a lot of "dirty air" is generated by the wheels spinning, and that disturbs the airflow leading to more drag.

On top of that first observation, the delta wing remain static throughout the experiment, meaning that the floor does not move. While in racing conditions, the floor under a race car moves and that allows for ground effect underneath the car. Ground effect is a very efficient manner to generate downforce with very little additional drag. On our LFS23 concept, the sidepods and the diffusor take advantage of the ground effect phenomenon in order to generate a lot of downforce. All of that additional downforce could not be generated by the scaled model in these conditions.

Nonetheless, this experiment allowed to have a first approximation of the race car performance. There is a clear difference of performance between the model with the whole aerodynamic package and without, with a Cl/Cd value of 3,4 compared to 1,8 respectively. One can also observe that each aerodynamic component contributes significantly to the production of downforce (see section 5.4.1).

When designing our car, the Cl/Cd value is on of the most important metrics to evaluate the performance of our design, according to our simulations the LFS23 car has a Cl/Cd value of 4,5 for a speed of 15m/s. While this experiment would predict a Cl/Cd of 3,4 for the real car at a driving speed of 1,5m/s.

Indeed, if we want to compare these experiments with real life behaviour, the similarity condition needs to be matched (section 2.5). If we wanted to match the LFS23 car at its average speed of 15m/s, the model would have to be tested in a windtunnel where the inlet speed is 150m/s, which would not be sustainable for the model obviously.

6.4.2 Drag Reduction System

Along with the standard model experiments, I chose to do some more tests with 4 sets of rear wings that were designed to minimise the amount of drag generated by the car. According to our simulation, the rear wing is responsible for up to 65% of the drag generated overall. Reducing the drag of the car is interesting for us in two racing categories.

First the acceleration where the car has to start from standstill and drive 70m as quickly as possible. The other racing event being the Endurance where we have to drive 22km, minimising drag there allows for energy savings which were needed for Lund Formula Student this year in order to safely cover the distance.

Although I do not trust the exact values of the drag forces generated by the model because I believe there is a multiplying constant missing, I still believe of the tendencies between results in a similar configuration. The tables in the section 5.1 suggest that the minimum of drag would be achieved for an AoA of -6°.

It turns out when testing the different rear wings that the minimum amount of drag was generated by the one with the secondary wing elements being at 0° AoA. In that configuration the Cd value is 0,320 while for the same inlet speed and the standard aerodynamic package, the Cd value is 0,816.

Using a laptime simulation software, and choosing a track layout where we run some physical tests with our race car, I chose to compare the energy consumption of the car with the two different Cd values.

Over the course of one lap on the Lockarp go-kart track, the car in its standard configuration (i.e Cd=0,816) consumed 0,041 kWh while in the DRS configuration, the car consumed 0.014kWh.

Running with the secondary elements of the rear wing at 0° of AoA reduces significantly the energy consumption of the car, but it would also reduce the amount of downforce generated by a lot, probably leading to slower lap times.

Using this experiment and their results, it comforted the Lund Formula Student team to have a rear wing configuration with both secondary elements being at 0° of AoA on the real car. I am really happy and proud that the team put their trust in my results to decide on the configuration of our rear wing. This proves that the scaled model can be used to assess the performance of different designs in a very time-efficient manner, and lead to concept decisions. Below is a picture of the actual LFS23 race car, in its minimal drag configuration :

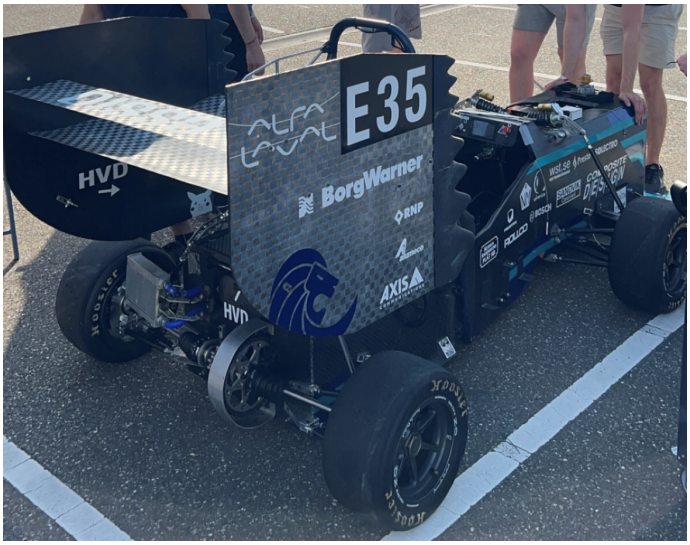

Figure 6.1: LFS23 car - DRS configuration

6.5 Particle Image Velocimetry

The last experiment I wanted to carry out was with Particle Image Velocimetry. In the previous windtunnel (in Ljungbyhed), I already had the opportunity to use smoke machines in order to visualise the airflow around the car. One could easily observe the wake of the car generated mainly by the rear wing as can be seen here:

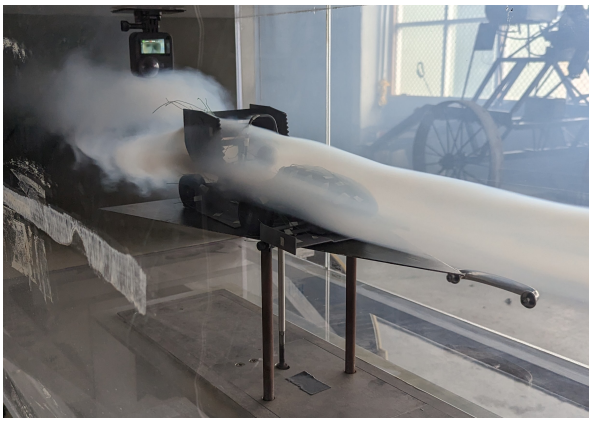

Figure 6.2: Scaled model wake

Then, the use of the smoke generator was only qualitative, I could not draw any tangible results from these observations. Therefore I wanted to try the PIV experiment to now use the smoke in a qualitative manner. As I explained earlier in the section 5.5, the experiment did not work. I think that there are several reasons to that failed attempt, the first one being the relative positioning of the camera and the model.

My initial ambition was to capture the airflow around the whole car in a single picture, and with the space constraints, each picture corresponded to a rectangle of 212mm by 163mm. Each interrogation area represented a square with a side of 10,24mm.

I believe that this was my first mistake, because the smoke particles were very very thin, therefore when the smoke was flowing from the inlet, there was smoke particles in basically each pixels of the camera, therefore not being able to tell how particles move between the first picture and the second just after.

While the camera positioning was an avoidable mistake that could be fixed, as well as having a better adjustment of the contrast in the picture taken, there was an other problem that I don't think could be solved with the time I had left before handing my master thesis. As the windtunnel is an open return windtunnel, the air pushed from the outlet circulates again in the room before going back into the inlet.

This meant that the smoke that initially went into the inlet started to fill the room very quickly. Within 2 minutes of experiments the whole room was in a thick fog, meaning that the camera could not take any proper pictures anymore, all of the shots ended up being blurred by the smoke particles outside of the test section.

To avoid that problem and have exploitable results, I believe the windtunnel would have to be changed so that either it becomes a closed loop, but the better option would probably be that there is a duct at the outlet of the windtunnel, preventing the smoke from filling the lab room.

7 Conclusion

7.1 Conclusion

Through this work on my master thesis, I have managed to showcase how we could combine 3d printing and windtunnel testing in the context of formula student. Using the CFD software starCCM+ and measurements on an airfoil shape, I managed to confidently confirm that are simulation parameters allow for accurate results. What I think is the most important on the overall work is regarding the scaled model. I am convinced that this tool can be a great asset when designing an aerodynamic package. It represents a very time efficient manner to evaluate different concepts that can show similar performances on a CAD software.

Thanks to my experiments, I contributed to the choice of our rear wing configuration when trying to minimise the amount of drag. I am very thankful for putting their trust in my results and that further proves how working with a similar scaled model in the future could prove beneficial for the Lund Formula Student team or any other. In my opinion this work can serve as a baseline for the coming years of aerodynamic design, but the experiments could be improved significantly.

7.2 Recommendations for future work

The CFD parameters that have been tested in this paper were the turbulence models as well as the boundary layer meshing. An other parameter that could be looked into is how the refinement of the wake behind the car is made, to try and optimise the results and the computing efficiency of the simulations.

Regarding the experiments with the scaled model, a second version could be made with spinning wheels using bearings. In that case, there should also be a custom "treadmill" below the scaled model to simulate a moving floor. With spinning wheels and a rolling floor, the behaviour of the scaled model would be much more representative of the formula student car in racing conditions. One should always remember that the speed of the rolling floor should be equal to the inlet speed of the windtunnel to have the correct physical behaviour.

Lastly, the Particle Image Velocimetry experiment could be reiterated. But as I explained earlier in the section 6.5, the current configuration of the windtunnel accessible in Lund is not prone to this type of experiment as it is an open return windtunnel. In my opinion a Formula Student team would spend a lot of energy and time to successfully conduct a PIV experiment, with little to no significant data that could be used for designing.

It could provide some information regarding the attachment of the airflow around the car, but that can already be estimated with bare eyes when watching smoke flow around the body of the model. As time is one of the most precious resources in the context of Formula Student, I would suggest to concentrate efforts into CFD correlation and scaled model force measurements.

References

[1] Versteeg, H.K. and Malalasekera, W. *An Introduction to Computational Fluid Dynamics*. Pearson Education Limited, 2007. ISBN: 9780131274983.

[2] S.B. Pope. *Turbulent Flows*. Cambridge, UK: Cambridge University Press, 2003. ISBN: 9780521598866.

[3] S.R. Almaras P.R. Spallart. *A one-equation turbulence model for aerodynamic flows*. American Institute of Aeronautics and Astronautics, 1992.

[4] Tsan-Hsing Shih et al. "A new k-ε eddy-viscosity model for high Reynolds number turbulent flows—Model development and validation". In: *Computers & Fluids* (1995).

[5] F. R. Menter. "Two-Equation Eddy-Viscosity Turbulence Models for Engineering Applications". In: *AIAA Journal* (1994).

[6] Anderson, J.D., Jr. *Fundamentals of aerodynamics*. New York, NY: McGraw-Hill Education, 2011. ISBN: 9781259010286.

[7] S. Gudmundsson. *General aviation aircraft design: applied methods and procedures*. Oxford, UK: Butterworth-Heinemann, 2014. ISBN: 9780123973085. DOI: https://doi.org/10.1016/C2011-0-06824-2.

[8] Anderson, J.D., Jr. *Introduction to flight*. New York, NY: McGraw-Hill Education, 2016. ISBN: 9780078027673.

[9] Virtual Amrita Laboratories Universalizing Education. *Wind Tunnel - Pressure*. https://vlab.amrita.edu/?sub=77&brch=297&sim=1671&cnt=3605. 2015.

[10] National Aeronautics and Space Administration. *Open Return Wind Tunnel*. https://www.grc.nasa.gov/www/k-12/airplane/tunoret.html.

[11] Ganesh Madivaanan A S M Al-Obaidi. *Investigation of the Blockage Correction to Improve the Accuracy of Taylor's Low-Speed Wind Tunnel*. Journal of Physics: Conference Series, 2022.

[12] J. Kompenhans M. Raffel C.E. Willert. *Particle Image Velocimetry: A Practical Guide*. Berlin: Verlag, 1998.

[13] Daniel Côté Sung Min Choi Wi Han Kim. *Blood cell assisted in vivo Particle Image Velocimetry using the confocal laser scanning microscope*. 2011.

[14] Bernhard Wieneke. “PIV Uncertainty Quantification and Beyond”. PhD thesis. 2017. DOI: 10.13140/RG.2.2.26244.42886.

[15] Cadence CFD Solutions. https://resources.system-analysis.cadence.com/blog/2023-computing-boundary-layer-thickness-in-cfd-analysis.

[16] James J. Guglielmo Michael S. Selig. *High-Lift Low Reynolds Number Airfoil Design*. University of Illinois, USA: Journal of Aircraft, Volume 34, 1997, p. 77.